Electrochemical conversion of CO_2 using metal-organic framework catalysts

Rodrigo Andrés Espinosa-Flores [a], Martín Daniel Trejo-Valdez [a,*],
María Elena Manríquez-Ramírez [a], Francisco Javier Tzompantzi-Morales [b]

[a] *Instituto Politécnico Nacional-ESIQIE, Laboratorio de Investigación en Nanomateriales y Energías Limpias, Edificio Z-5, P.B., Zacatenco, Gustavo A. Madero, Ciudad de México, 07738, Mexico*
[b] *Departamento de Química, Área de Catálisis, Universidad Autónoma Metropolitana – Iztapalapa, Av. San Rafael Atlixco No. 189, C.P. 09340, Ciudad de México, Mexico*

ARTICLE INFO

ABSTRACT

Metal-organic frameworks (MOFs) have been an excellent platform for carbon dioxide reduction reactions (CO_2RR). In this work, the feasibility of electrochemical reduction of CO_2 to obtain C_2-deep value-added products was investigated by the preparation of Mg-containing MOF-74 samples combined with transition metal cations (Ni^{2+}, Co^{2+} and Zn^{2+}). The prepared MOFs were used as electrocatalysts in CO_2RR. Chronoamperometric analysis coupled to ATR-FTIR spectroscopy was employed to characterize the CO_2 reduction products and subsequently via ^1H NMR. Although an isostructural crystalline structure was observed in all synthesized MOFs, the pore diameter distribution was significantly affected due to the Mg coordination along with each transition metal nuclei with the organic ligand to form the MOF-74. Our results showed that Mg-containing MOF-74 electrocatalysts combined with Ni, Co and Zn ions successfully reduced CO_2 to C_2-deep products, while the monometallic Mg-MOF-74 showed only CO_2 mineralization. An ester acetate, isopropyl alcohol, and formic acid were produced by Mg/Ni-MOF-74; isopropyl alcohol was provided by Mg/Co-MOF-74, and ethanol was generated by Mg/Zn-MOF-74. We observed that the change of the transition cation was a key factor in the selectivity of the obtained products, while the degree of Mg ions effectively incorporated into the MOF structure tuned the porosity and the electrocatalytic activity. Among them, Mg/Zn-MFOF-74 showed the highest Mg content loaded after synthesis and thus the most favorable electrocatalytic behavior towards CO_2 reduction.

1. Introduction

Current scientific research focuses on slowing the environmental impact of the main greenhouse gas, carbon dioxide (CO_2) [1]. To address this problem, the most promising solution is to capture CO_2 and subsequently convert it into value-added chemicals using an electrochemical approach, as it is an easily manipulated and controllable method that also operates under ambient conditions [2,3]. Among several classes of electrocatalysts, metal-organic frameworks (MOFs) stand out as a new class of hybrid materials constructed from the association of inorganic building blocks connected by organic linkers, with potential properties favorable for CO_2 reduction,

such as highly tunable pore size to enhance diffusion. In addition to their outstanding chemical flexibility, these properties put MOFs ahead of other well-known electrocatalysts [4–6]. Although there are several studies using monometallic MOFs as electrocatalysts, bimetallic organometallic frameworks outperform the catalytic activity of monometallic organometallic frameworks due to a synergistic effect [7–9]. However, the studies on bimetallic MOFs for electrochemical CO_2 reduction reaction (CO_2RR) based on alkaline-earth metals have remained comparatively scarce [7,10,11]. Porous frameworks based on alkaline-earth metals offer gravimetric advantages for storage applications, for example, such as the superior CO_2 adsorption of Mg-MOF-74 over other selected metal-organic frameworks [12]. Indeed, they have become particularly attractive due to their selectivity for adsorbing targeted molecules such as carbon dioxide (CO_2) over other undesired molecules [1]. This suggests that some classes of MOFs possess a pore network favorable for selective adsorption of target molecules.

Regarding the bimetallic catalyst approach, CO_2-related catalytic and photocatalytic studies have shown that MOF-74 used as a bimetallic catalyst could further improve its catalytic performance toward CO_2 reduction and regulate the energy barrier of the intermediate CO_2-derived product, although it has not yet been tested in the electrocatalytic field. Furthermore, the correlation between porosity and CO_2-derived electrocatalytic activity in Mg-containing bimetallic MOFs is still unexplored [7–9,13]. In this work, we investigate the effect of magnesium incorporation in MOF-74 structures on its porosity and electrocatalytic performance of the synthesized materials.

Although carbon monoxide (CO) and formate (HCOOH) are routinely reported in several works using monometallic M-MOF electrocatalysts (M = Co, Ni, and Zn), the desired goal is to obtain C_2-deep-reduction products, such as ethanol (CH_3CH_2OH), isopropanol ($CH_3CH(OH)CH_3$), among others [7,14,15]. A second goal of our work is to obtain C_2-deep-reduction products by using Mg-containing bimetallic MOF-74 electrocatalysts. This report demonstrates that magnesium coupled with the transition metal (Co, Ni and Zn) on MOF-74 bimetallic compounds can further reduce CO_2 to C_2-deep reduction products like alcohols and acetate esters. Furthermore, we show that depending on the effective Mg content left in the bimetallic MOFs, the pore network is tuned to an extent that favors mass transfer during the CO_2-reduction proccess. In addition, we present an integral study including the CO_2-derived electroactivity, the electronic interaction, the charge-transfer resistance, the textural data, and the structural characterization for the Mg-based bimetallic electrocatalysts.

2. Experimental

2.1. Synthesis of monometallic Mg-MOF-74

Mg-MOF-74 compound was synthesized under solvothermal conditions and according to a previous report [16]. In summary, to a solid mixture of 2,5-dihydroxyterephtalic acid (0.111 g) (H_4DOBDC, 99%, Sigma-Aldrich®) and $Mg(NO_3)_2 \cdot 6H_2O$ (0.0032 mol) (99%, Sigma-Aldrich®), a 15 : 1 : 1 (v/v/v) mixture of dimethylformamide (DMF 99.8%, Sigma-Aldrich®), ethanol (99.9%, Fermont) and distilled water were added, respectively. The solution was mixed stirring vigorously for 15 min and the mixture was transferred to a Teflon-lined steel autoclave, which was sealed and heated at 110 °C for 48 h. After cooling at room temperature, the supernatant was poured off and the resulting crystals were harvested and washed twice with ethanol prior to drying in a vacuum desiccator.

In a similar way and according to the target bimetallic MOF synthesis, the following mixtures were prepared and used as solvothermal precursor solutions.

2.1.1. Synthesis of bimetallic Mg/Zn-MOF-74

To a solid mixture of 2,5-dihydroxyterephtalic acid (0.482 g) (H_4DOBDC, 99% Sigma-Aldrich®), 0.0032 mol of $Mg(NO_3)_2 \cdot 6H_2O$ (99%, Sigma-Aldrich®) and 0.0079 mol of $Zn(NO_3)_2 \cdot 6H_2O$ (98%, Sigma-Aldrich®), a 1:1:1 (v/v/v) mixture of dimethylformamide (DMF 99.8%, Sigma-Aldrich®), ethanol (99.9%, Fermont) and distilled water were added, respectively. The solution was mixed until homogeneous.

2.1.2. Synthesis of bimetallic Mg/Co-MOF-74 and Mg/Ni-MOF-74

Mg/Co-MOF-74 and Mg/Ni-MOF-74 were synthesized following the same procedure as Mg/Zn-MOF-74 except for the addition of 0.012989 mol of $Co(NO_3)_2 \cdot 6H_2O$ (98%, Sigma-Aldrich®) or 0.013 mol of $Ni(NO_3)_2 \cdot 6H_2O$ (98%, Sigma-Aldrich®) instead of 0.0079 mol of $Zn(NO_3)_2 \cdot 6H_2O$ (98%, Sigma-Aldrich®).

2.2. Characterization techniques

The attenuated total reflectance Fourier transform infrared spectra (ATR-FTIR) of the samples were recorded in an FTIR spectrophotometer (PerkinElmer Spectrum Two model). The samples were scanned over the spectral region from 500 to 4000 cm^{-1}.

Powder X-ray diffraction (XRD) patterns were recorded on a Rigaku Miniflex 600 diffractometer using Cu-Kα radiation (1.5406 Å) source in the range of 3°<2θ< 30° at a scan rate of 4°/min.

The morphology and surface texture of the samples, as well as their elemental analysis, were analyzed using a Field Emission Scanning Electron Microscope (Schottky JSM-7800 F). Samples were imaged using a secondary electron detector at an acceleration voltage of 2.0 kV under an ultra-high vacuum. The samples dimensions were measured using the ImageJ software.

The X-ray photoelectron spectroscopy (XPS) measurements were performed on a THERMO Scientific K-Alpha spectrometer using an Al Kα radiation (1486.6 eV) as the X-ray source, and a hemispherical electron analyzer. Experimental peaks were deconvoluted into their components using mixed Gaussian-Lorentzian functions and a non-linear square fitting algorithm. Then, Shirley's background
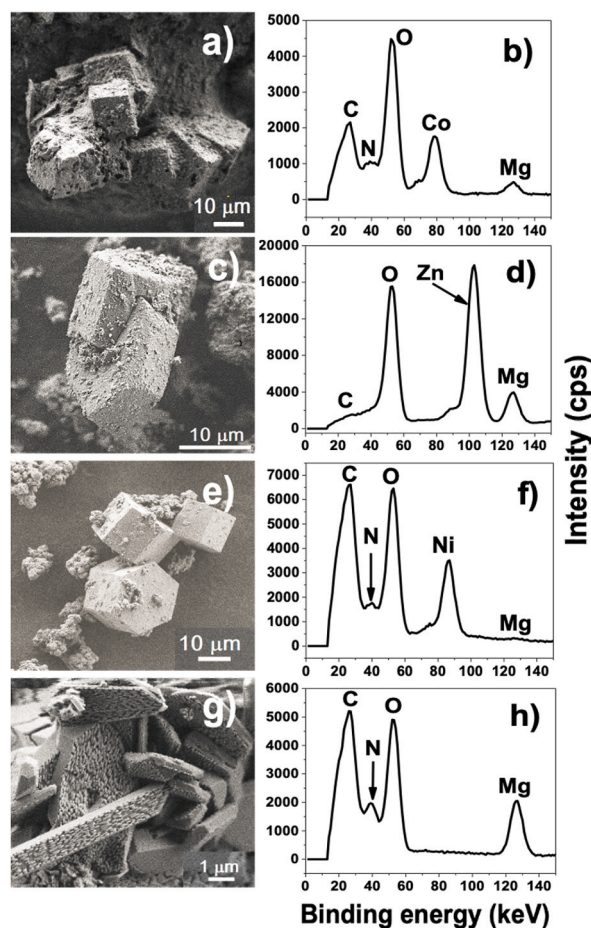
Fig. 1. Left: Scanning electron microscope micrograph images of the MOF morphologies. Right: EDS (Energy Dispersive Spectroscopy) spectra of the MOFs. (a), (b): Mg/Co-MOF-74. (c), (d): Mg/Zn-MOF-74. (e), (f): Mg/Ni-MOF-74. (g), (h): Mg-MOF-74.

subtraction was applied. A quantitative elemental analysis was performed using this technique.

The specific surface area, average pore diameter, and pore volume were determined from N_2 adsorption-desorption isotherms. The samples were thermally treated in a vacuum at 80 °C for 12 h. The N_2 gas adsorption-desorption was carried out at 77.3 K using a BELSORP-max equipment. The specific surface areas were determined using the Brunauer-Emmet-Teller (BET) method, while the pore diameter and pore volume were calculated from the desorption isotherms and following the Barret-Joyner-Halenda (BJH) method.

The photoluminescence (PL) analysis was carried out on a FS-2 Fluorescence Spectrometer Scinco equipment, and the spectra was obtained at an excitation wavelength of 254 nm in the range of 400–650 nm.

2.3. Electrochemical test and product analysis

Cyclic voltammetry (CV) and Electrochemical Impedance Spectroscopy (EIS) were carried out on an AUTOLAB potentiostat/galvanostat PGSTAT302 N, in a three-electrode configuration cell using an ink-coated MOF DROPSENS DRP-C110 as the working electrode, a platinum wire as the counter electrode, and standard hydrogen electrode (S.H.E.) as the reference electrode in a 0.1 M KNO_3 aqueous electrolyte. The working electrode is circular, with a diameter of 0.4 cm and an effective geometric area of 0.1257 cm^2. The dimensions of the strip are $3.4 \times 1.0 \times 0.05$ cm (length × width × height). To prepare the electrode, 0.175 g of MOF sample and 50 μL of Nafion® were dispersed in 800 μL of distilled water and 150 μL of isopropanol by sonication for 10 min to form a homogeneous ink. For Cyclic Voltammetry (CV): scans were performed in the potential range from 1.0 to −2.0 V vs SHE at 10 mV/s; Electrochemical Impedance Spectroscopy (EIS) was performed using a frequency response analyzer (FRA) connected with Metrohm Autolab PGSTAT302 N potentiostat within the frequency range of 0.1 Hz–100 Hz, at open circuit potential (OCP). Experimental control and data acquisition were carried out using Nova 1.10 software. Nyquist plots were obtained and compiled by electrochemical impedance spectroscopy (EIS) for working electrodes coated with MOFs samples and immersed in N_2-saturated and CO_2-saturated KNO_3 0.1 M electrolyte. To address the data analysis, the impedance data were fitted to an equivalent circuit consisting of electrolyte resistance, R_Ω, charge transfer resistance, R_{CT}, constant-phase element admittance, Y_0, and electrical double-layer capacitance, C_{DL}. In addition, the Kronig-Kramers (KK) test can be used to check whether the system measured in time and linear. Therefore, the KK test was performed
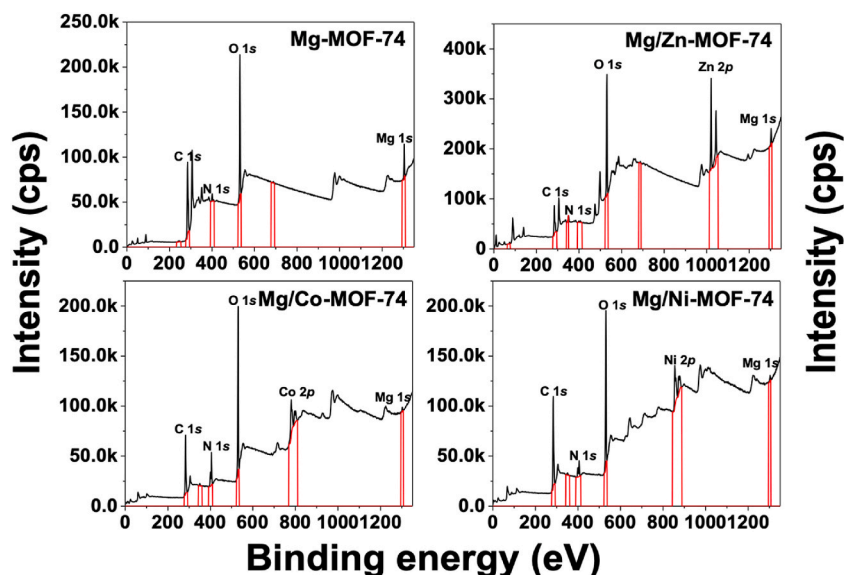
Fig. 2. General X-ray photoelectron spectra of the MOFs compounds.

to check for goodness of fit (χ^2) and the results were attached to the equivalent circuits, respectively. A small χ^2 value usually indicates a good fit. This approach was carried out using the NOVA 1.10 software for both N_2-saturated electrolyte and CO_2-saturated KNO_3 0.1 M electrolyte.

Chronoamperometry coupled to ATR-FTIR spectroscopy was used to analyze CO_2RR-derived products. This test was carried out on an AUTOLAB potentiostat/galvanostat PGSTAT302 N but with a different cell arrangement. A custom-made three electrode cell that fitted on top of the ATR crystal was machined from polytetrafluoroethylene (PTFE) fitted with a glassy carbon rod as counter electrodes and quasi-reference. The working electrode was a 3 mm diameter graphite electrode (GE). Since inorganic nitrate ions provide a broad and intense IR band near 1400 cm^{-1}, resulting from out-of-phase stretching for nitrate-containing compounds, for these spectroelectrochemical tests the KNO_3 electrolyte was replaced by KOH electrolyte, since the spectrum obtained will not have interfering bands. It is indeed worth mentioning that a background was subtracted before collecting the ATR-FTIR scans. An aqueous solution containing 0.1 M KOH electrolyte was degassed beforehand under sonication for 20 min, and then N_2 was bubbled into the electrolyte for 20 min to purge O_2. This N_2-saturated solution was transferred to the custom-made PTFE three-electrode cell and a background spectrum was collected at this point. All spectra were subtracted with the background. Next, CO_2 was bubbled for 20 min and then an IR spectrum was recorded. This test was performed for 30 min at −1.6 V vs GE under 0.1 M KOH CO_2 saturated aqueous electrolyte and data acquisition was conducted using Nova 1.10 software. Potential was applied to the working electrode, and IR spectra were collected every 3 min ^{1}H Nuclear Magnetic Resonance spectroscopy was used to identify CO_2RR-derived liquid products produced during constant potential electrolysis. Liquid products were recorded on a Bruker Avance III NMR spectrometer operating at 400 MHz ^{1}H using deuterated water (D_2O) as an internal standard. ^{1}H nuclear magnetic resonance (NMR) spectra analysis and collection was performed on Mestrenova software.

3. Results and discussion

3.1. SEM spectroscopy

The SEM micrographs showed MOFs samples with geometrically derived shapes (Fig. 1a, c, e, g). The morphology of Mg/Co-MOF-74 is shown in Fig. 1a and corresponds to a uniform decoration of cubic particles with a porous structure on the surface. In Fig. 1c, Mg/Zn-MOF-74 has a hexagonal disc-shaped structure, intercalated within a hexagonal prism-shaped structure, while Mg/Ni-MOF-74 in Fig. 1e shows a regular hexagonal prism-shaped structure. When compared Mg-MOF-74 to the regular-shaped bimetallic MOFs samples, an irregular geometrical morphology is observed, however large and elongated stacked rods predominate (Fig. 1g), with tube-like shapes that may serve as adsorbents. Qualitative spectral analysis of MOFs (Fig. 1b, d, f, h) was conducted to confirm the existence of the corresponding elements (Mg, Ni, Co and Zn) in the MOFs samples. According to the relative intensity of the Mg content in each of the bimetallic electrocatalysts, the Mg content increased with the trend Mg/Ni-MOF-74 < Mg/Co-MOF-74 < Mg/Zn-MOF-74. The Mg content in the Mg/Zn-MOF-74 structure was considerably higher than in Mg/Co-MOF-74 and Mg/Ni-MOF-74 structures. Note that Mg content in the Mg/Ni-MOF-74 structure was considerably lower than the Ni content. This showed that Ni^{2+} coordinated more easily with H_4DOBDC to form MOF-74 than Mg; similarly for Co^{2+} ions. However, the coordination of the Mg/Ni-MOF-74 is distorted since Mg^{2+} replaces some Ni^{2+} in the MOF-74 lattice [8]. In contrast, the Zn^{2+} coordination with H_4DOBDC to form MOF-74 did not mask the Mg^{2+} coordination with H_4DOBDC during its synthesis process, as evidenced by the Mg content in Mg/Zn-MOF-74 (Fig. 1d). It can

Table 1

Quantitative elemental analysis of the MOFs. W (%) = % Weight. A (%) = % Atomic.

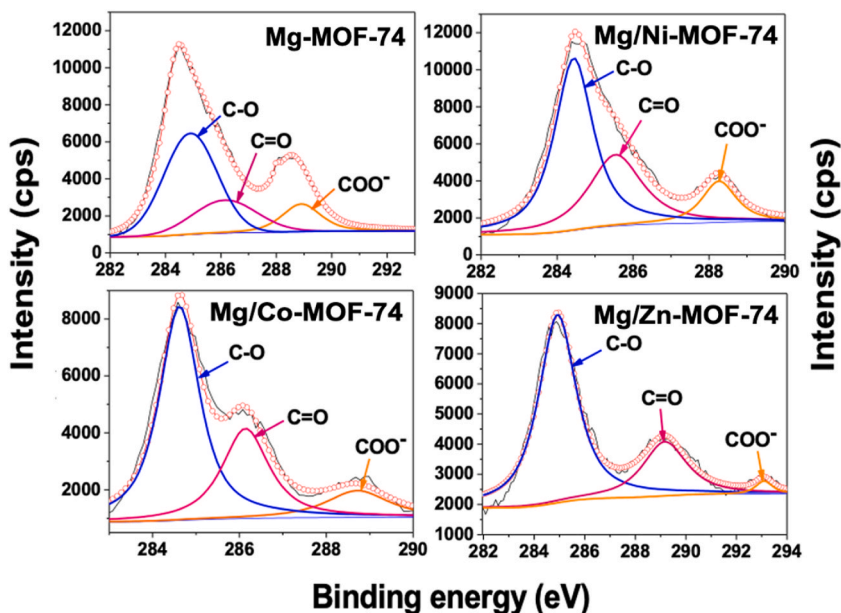| Element	Mg-MOF-74		Mg/Ni-MOF-74		Mg/Co-MOF-74		Mg/Zn-MOF-74	
	W (%)	A (%)	W (%)	A (%)	W (%)	A (%)	W (%)	A (%)
C 1s	50.1	57.8	41.2	54.0	28.8	39.4	21.7	35.7
O 1s	39.1	35.3	32.4	32.2	39.0	39.8	41.0	49.2
Mg 1s	7.5	4.4	1.0	0.7	0.9	0.6	4.3	3.5
N 1s	3.3	3.3	7.2	8.2	13.2	15.5	1.5	2.1
Ni 2p	0.0	0.0	18.2	4.9	0.0	0.0	0.0	0.0
Co 2p	0.0	0.0	0.0	0.0	18.2	5.1	0.0	0.0
Zn 2p	0.0	0.0	0.0	0.0	0.0	0.0	31.6	9.6

Fig. 3. Core-level spectra of C 1s of the MOFs.

be concluded that, depending on the metal core, the coordination distortion affects the synthesis of the Mg-based bimetallic MOF-74, resulting in different Mg content. This Mg content within the bimetallic MOF-74 confers unique properties, such as pore volume tuning for CO_2 mass-transfer and lower charge-transfer resistance. N and C elements are almost absent in the Mg/Zn-MOF-74 elemental analysis, besides, they could not be detected in the elemental mapping which was performed under a punctual analysis (Fig. 1d). Nevertheless, the occurrence of these elements in MOF Mg/Zn-MOF-74 are confirmed in X-ray photoelectron spectroscopy (XPS) characterization in Fig. 2.

3.2. X-ray photoelectron spectroscopy (XPS) characterization

Fig. 2 shows the XPS spectra of four kinds of MOF-74. It can be seen they contain, respectively, four elements, namely metals (Ni, Co, Zn and Mg), C, O and N. An elemental quantitative analysis for each MOF is presented in Table 1. As depicted in Fig. 1b, d, f, Mg/Co-MOF-74 and Mg/Ni-MOF-74 displayed a lower Mg content than Mg/Zn-MOF-74. This statement is confirmed by the elemental Mg content in all the bimetallic MOFs (Table 1). Mg/Zn-MOF-74 has a Mg content comparable to Mg-MOF-74, indicating that Mg has been successfully incorporated into its lattice. Fig. 3 depicts peaks representing C–O, CO and COO⁻, respectively. The presence of these functional groups is due to the carbonate species which absorbed on the MOFs surface and to the MgO (magnesium oxide) basic properties and its ability to adsorb CO_2 [17]. It is noteworthy there is a displacement at higher binding energies for Mg/Zn-MOF-74 COO^- species. As evidenced in Fig. 3, Mg/Zn-MOF-74 has the highest Mg content among bimetallic electrocatalysts, since each metallic nucleus along with Mg coordinates more preferentially to H₄DOBDC than others. This amount of Mg^{2+} could isolate the Zn^{2+} ions in the metal-to-ligand (M-oxo) chains in such a way that the oxygen gained more electron withdrawing power, shifting the COO^- species to a higher binding energy. Fig. S1 (shown in supporting information) illustrates the XPS of O 1s where peaks at binding energies of 531 and 533 eV represent oxygen bonded to metals and 532.4 eV is assigned to the oxygen connected to carbon, confirming the successful metal-to-ligand coordination [18]. Ni 2p of Mg/Ni-MOF-74 has two main peaks, concentrated around 873.0 eV and 856.0 eV, corresponding to Ni $2p_{1/2}$ and Ni $2p_{3/2}$ respectively; the other two peaks located at 879.6 eV and 860.9 eV correspond to the

Table 2
Textural properties of bimetallic and monometallic MOFs.

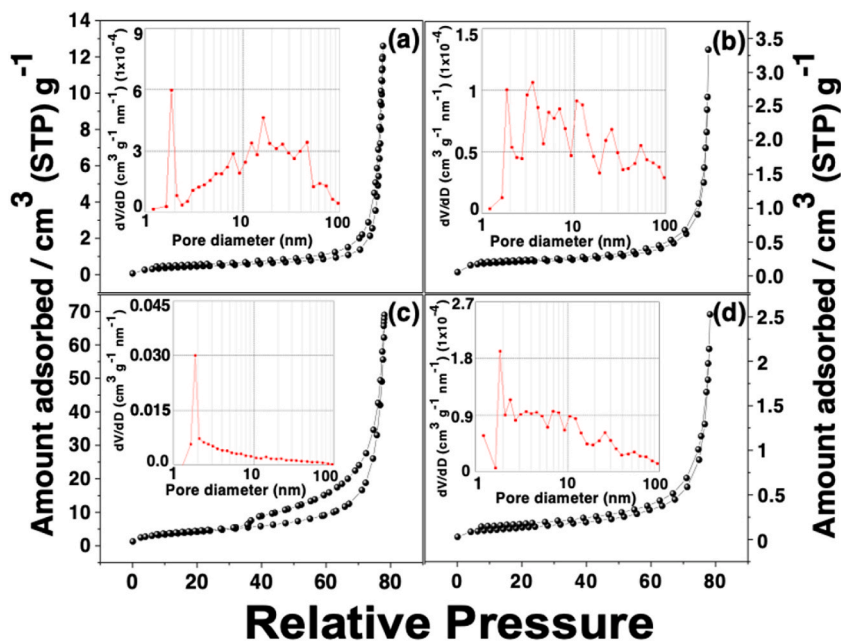| Electrocatalyst	Surface area (m^2/g)	Pore volume (cm^3/g)	Pore diameter (nm)
Mg-MOF-74	85.49	0.3776	17.667 ± 0.530
Mg/Ni-MOF-74	108.03	0.4649	17.214 ± 0.516
Mg/Co-MOF-74	44.8	0.3656	14.54 ± 0.436
Mg/Zn-MOF-74	13.47	0.0677	20.116 ± 0.603

Fig. 4. N_2 adsorption-desorption isotherms at 77.3 K and pore diameter distributions (insets) of (a) Monometallic Mg-MOF-74, (b) Mg/Ni-MOF-74, (c) Mg/Zn-MOF-74 and (d) Mg/Co-MOF-74, respectively.

satellite peaks of Ni $2p_{1/2}$ and Ni $2p_{3/2}$, which are characteristic of Ni^{2+} peak (Fig. S2 of supporting information). A similar analysis may be performed for Mg/Co-MOF-74 and Mg/Zn-MOF-74, indicating that Co and Zn are divalent (Figs. S3, S4 of supporting information) [19,20]. Therefore, they could act as active sites for electrocatalysis, having their valence electrons available for the faradaic processes.

3.3. Pore and textural characterization

The Brunauer-Emmet-Teller (BET) surface area and the pore volume were investigated to find a possible correlation with the electrocatalytic activity of the MOFs. Results are reported in Table 2 and Fig. 4. A multimodal pore diameter distribution was presented for Mg/Ni-MOF-74, Mg/Co-MOF-74 and Mg-MOF-74, revealing the existence of macropores and mesopores for these materials. According to Fig. 4(a), (b), and (d), Mg-MOF-74, Mg/Ni-MOF-74 and Mg/Co-MOF-74 exhibited a type II isotherm given on macroporous adsorbents, with a type H3 loop. They also exhibited a multimodal pore diameter distribution. Indeed, the Mg/Ni-MOF-74 has a broader distribution of pore diameters. This could be explained by the distortion in the coordination process discussed above. However, it is worth noting that the isotherm for Mg/Zn-MOF-74 shows a unimodal pore diameter distribution and its hysteresis loop is wider than the others (Fig. 4(c)). This hysteresis loop is indicative of the presence of a large number of mesopores, which is beneficial for the mass transfer during the electrocatalytic process [21,22]. In fact, it has the largest pore diameter among all MOF-derived electrocatalysts, as can be seen in Table 2. The Brunauer-Emmet-Teller (BET) surface area and the pore volume decrease with the trend Mg/Ni-MOF-74 > Mg-MOF-74 MOF > Mg/Co-MOF-74 > Mg/Zn-MOF-74. This may be due to the distortion of the coordination environment resulting from the ease of coordination between the transition metal and the alkaline earth metal with the H_4BODC to form the corresponding MOF-74.

3.4. FTIR spectral characterization

The functional groups and characteristic bonds of the synthesized MOFs are revealed in the FTIR spectra (Fig. 5), where the shape as well as the frequency of the absorption bands are similar in the four MOFs. In the MOF spectroscopic field, the IR technique is useful to
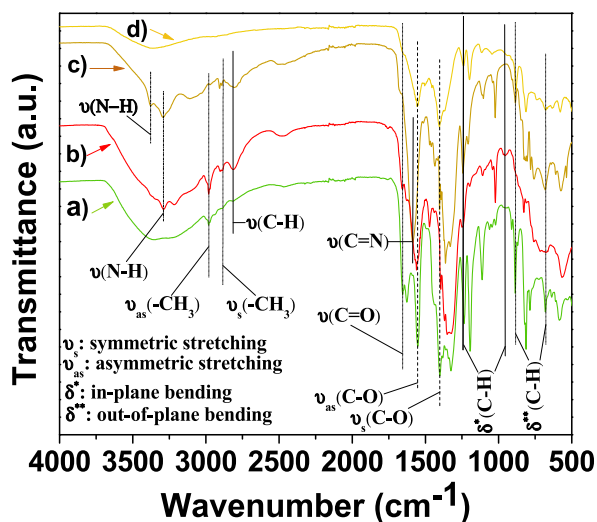
Fig. 5. FTIR spectra of: (a) Mg/Ni-MOF-74, (b) Mg/Co-MOF-74, (c) Mg-MOF-74 and (d) Mg/Zn-MOF-74.

corroborate the coordination between metal centers and organic linkers, since distinctive downshift of an absorption band can be observed as described below. The distinctive absorption band appeared at 1655 cm^{-1}, close enough as reported by Furukawa [23], attributed to CO bonding in the organic linker, which indicates it has a single-bond character due to the delocalization of the π electrons thereby weakening the carbonyl CO bond, which suggests that the carboxyl group has been deprotonated. Since the metal-carboxylate bond was cleaved, the strong coordination between the organic linker and the metal center is deduced. This argument is strengthened by the fact that the carbonyl group without a significant single-bond will stretch at a higher frequency than one with delocalized electrons [24].

The IR spectrum reflects the presence of benzene-carboxylates as organic linkers in the structure of electrocatalysts. The peaks from 955 to 1240 cm^{-1} correspond to in-plane C–H bending vibrations of the benzene ring. Moreover, the peaks located from 668 to 886 cm^{-1} are due to out-of-plane C–H bending vibrations, which belong to the aromatic rings of carboxylates [24]. The absorption bands at 1553 and 1404 cm^{-1} correspond to the asymmetric and symmetric stretching of dicarboxylate linkers, respectively [25]. The absorption bands between 2980 and 2890 cm^{-1} were attributed to the asymmetric and symmetric stretching of the –CH$_3$ group, respectively, and the CN bond stretch at 1585 cm^{-1} [26–28]. The band at 2814 cm^{-1} corresponds to the C–H bond stretching, whose carbon is bonded next to the C $=$ O group [29]. The absorption bands ranging between 3376 and 3292 cm^{-1} were ascribed to the amine N–H bond stretching frequencies [30]. Thus, it is inferred that these peaks correspond to DMF molecules that are occluded as guest molecules within the pores of the MOF structure [31], which is noticeable for Mg/Co-MOF-74 and Mg-MOF-74 IR absorption profiles.

3.5. Structural characterization

For typical MOF compounds, XRD patterns were reported and inspection of 2θ values from 2° to 35° (for Cu Kα) is generally sufficient to identify whether or not the MOF material has been successfully produced [23]. Based on these reports, Fig. S5 (support information) displays XRD patterns of MOFs and shows Miller indices corresponding to the most representative crystallographic planes of MOFs. Since the four synthesized MOFs are isostructural, the four diffraction patterns are the same. The diffraction peaks are intense and sharp, indicating a satisfactory crystal structure in the synthesized materials.

Two noticeable diffraction peaks appear in the XRD pattern. The intensity of the first reflection at 2θ *(deg)* $= 6.88$ has been reported in previous reports and it corresponds to the (210) crystal face [8,9,15,25,31]. The intensity of the second reflection at 2θ *(deg)* $= 11.88$ corresponds to the (300) crystal face and indicates the topological structure as well the structure-preserving isomorphism is retained for the four synthesized MOFs [15]. The diffraction pattern reported by Senthil Kumar et al. shows high similarity with that obtained for the MOFs samples of this work, corroborating a MOF-type pattern for the synthesized materials [32]. The four diffraction patterns are consistent due to their isostructural form (as observed in Fig. S1 of supporting info), since the substitution of Mg by the transition metal does not affect the crystal structure of Mg-MOF-74, supporting the successful synthesis of bimetallic Mg-MOF-74 electrocatalysts. As reported by Ling et al. replacing Mg with the transition metal did not affect the crystal structure of Mg-MOF-74, supporting that bimetallic Mg-MOF-74 electrocatalysts were successfully synthesized [8]. However, there are differences in relative intensity as well as the reflection angles do not match perfectly between the diffraction patterns of the Mg/Zn-MOF-74 and Mg/Ni-MOF-74 samples compared to the Mg/Co-MOF-74 and Mg-MOF-74 samples. We suggest that this mismatch is due to the presence of guest molecules from the DMF solvent within the pores of the Mg/Co-MOF-74 and Mg-MOF-74 structures. This statement is confirmed by the characteristic IR absorption bands of the secondary amide of Mg/Co-MOF-74 and Mg-MOF-74 samples, as shown in Fig. 5.
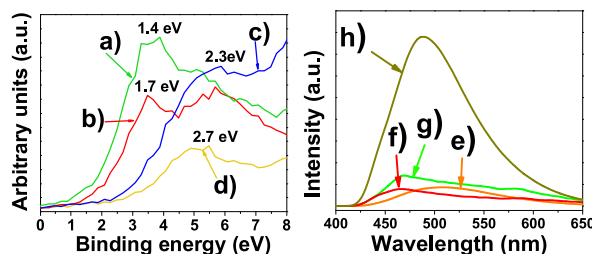
Fig. 6. Left: X-ray photoelectron band energy spectrum of the MOFs. (a) Mg/Ni-MOF-74, (b) Mg/Co-MOF-74, (c) Mg/Zn-MOF-74 and (d) Mg-MOF-74. Right: Photoluminescence spectra of the MOFs. (e) Mg/Zn-MOF-74, (f) Mg/Co-MOF-74, (g) Mg/Ni-MOF-74 and (h) Mg-MOF-74.
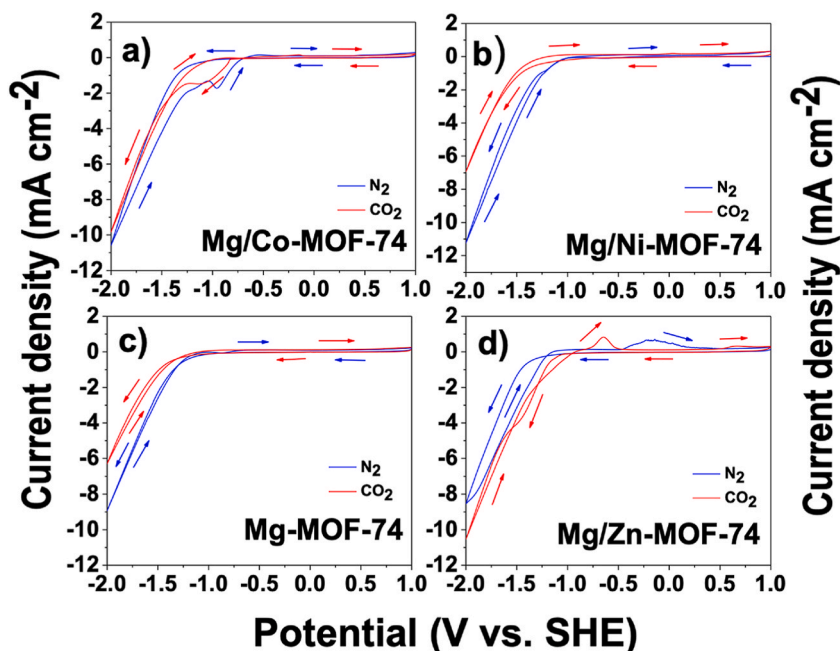

Fig. 7. Cyclic voltammogram curves for the MOFs in N_2-saturated and CO_2-saturated 0.1 M KNO_3 electrolyte. $E_0 = 1000$ mV, $E_1 = -2000$ mV, $E_2 = 1000$ mV. Scan rate: 10 mV/s (a) Mg/Co-MOF-74, (b) Mg/Ni-MOF-74, (c) Mg-MOF-74 and (d) Mg/Zn-MOF-74.

3.6. Optical characterization

The band energy was obtained from the XPS spectra as shown in Fig. 6 (left side). The results showed that the lowest band energy corresponds to Mg/Ni-MOF-74 and Mg/Co-MOF-74, whose magnesium content was lower than that of Mg/Zn-MOF-74 and Mg-MOF-74 compounds, as confirmed in Table 1 and Fig. 1b, d, f. This trend suggests that MOFs' energy band increased with magnesium content effectively incorporated into their lattices.

Photoluminescence emission spectroscopy revealed lower emission intensities for the bimetallic MOFs compared to the monometallic Mg-MOF-74. This fact was related to an increase in charge transfer and a decrease in charge carrier recombination (hole-electron pair) which increased the electrocatalytic efficiency. This is in agreement with the calculated band energy results, i.e. higher catalytic activity for bimetallic MOFs. There is a positive correlation between the high-energy band for the monometallic Mg-MOF-74 and its high photoluminescence intensity (Fig. 6, right side). Photoluminescence emission spectroscopy supports the increased recombination rate of photo-generated electron-hole pairs for Mg-MOF-74, offering a higher recombination rate for higher photo-luminescence intensity. Although this work does not address photocatalytic processes, there is a relationship with respect to electron mobility between photons and electrons and, considering these results, monometallic Mg-MOF-74 is expected to show the lowest electrocatalytic activity for the CO_2 reduction reaction compared to bimetallic MOFs.

3.7. Electrochemical CO_2RR analysis

3.7.1. DC voltammetry

For Mg/Co-MOF-74 electrocatalyst, in a N_2-saturated electrolyte (Fig. 7a), as the potential is scanned negatively, a capacitive

Table 3

Summary of the current densities achieved at −2 V (vs. SHE) in both N$_2$-saturated and $_2$-saturated KNO$_3$ 0.1 M electrolyte.CO

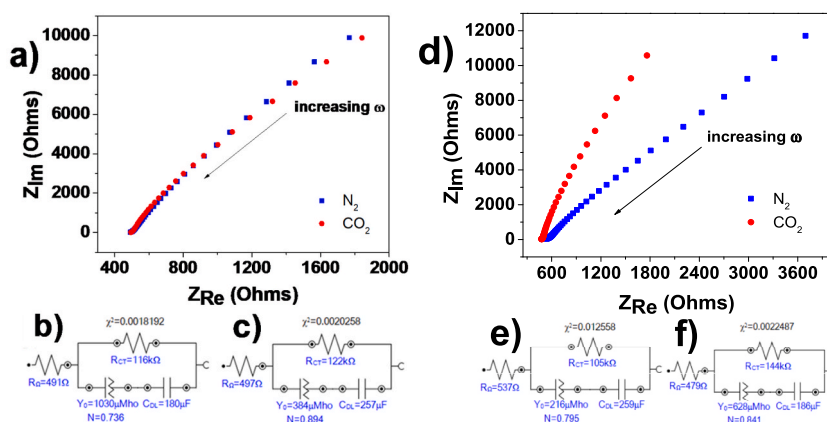| Working electrode	N$_2$	CO$_2$
	J$_{(-2V)}$ (mA cm^{-2})	J$_{(-2V)}$ (mA cm^{-2})
Mg-MOF-74	−8.688	−6.2710
Mg/Zn-MOF-74	−8.5071	−10.4663
Mg/Co-MOF-74	−10.5343	−9.7719
Mg/Ni-MOF-74	−11.1339	−6.8658

Fig. 8. (a), (d) Nyquist plot for Mg/Co MOF (left) and Mg/Zn MOF (right) in N$_2$-saturated and CO$_2$-saturated KNO$_3$ 0.1 M electrolyte with an AC amplitude of 10 mV and a frequency range between 100 Hz and 0.1 Hz. (b), (c), (e), (f) Equivalent electrical circuits defined from the electrochemical impedance spectroscopy data fitting for Mg/Co MOF (left) and Mg/Zn MOF (right). (b), (e) N$_2$-saturated electrolyte. (c), (f) CO$_2$-saturated electrolyte.

current is recorded until the potential becomes less positive than −0.96 V vs. SHE, when a cathodic current occurs due to the hydrogen evolution reaction (HER), showing a current density, J$_{(-2V)}$, of −10.53 mA cm^{-2} when the potential reaches −2 V (vs. SHE), as shown in Fig. 7a. This process is represented by the water reduction reaction as follows:

$$2H_2O + 2e^- \rightarrow H_{2(g)} + 2OH^-$$
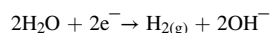
At the reverse scan, there is a cathodic peak at −0.958 V vs. SHE and an anodic peak at −0.533 V vs. SHE concerning NO$_3^-$ ions faradaic processes [33,34]. Similar results were obtained for the rest of MOF compounds in a N$_2$-saturated electrolyte.

The response in the CO$_2$-saturated electrolyte is also included in Fig. 7a. As the potential is scanned negatively, a capacitive current is recorded until the potential becomes less positive than −0.81 V vs. SHE, from which a cathodic current occurs until a cathodic peak arises at −1.14 V (vs. SHE), corresponding to NO$_3^-$ ions reduction. As the potential is scanned more negatively, there is an onset potential at −1.246 V (vs. SHE), from which the cathodic current continued to increase until the potential reaches −2 V (vs. SHE), showing a current density, J$_{(-2V)}$, of −10.53 mA cm^{-2}. At the reverse scan, there is an anodic peak at −0.15 V vs. SHE, associated with the oxidation of NO$_2^-$ ions [33].

The cyclic voltammogram of the Mg/Ni-MOF-74 electrocatalyst in the CO$_2$-saturated electrolyte is shown in Fig. 7b. In this voltammogram, a cathodic current occurs at −0.916 V (vs. SHE) ascribed to the CO$_2$ reduction reaction. Such cathodic current continued to increase until the potential reaches −2 V (vs. SHE), showing a current density, J$_{(-2V)}$, of −6.866 mA cm^{-2}.

The resulting cyclic voltammogram of the monometallic Mg-MOF-74 electrocatalyst is shown in Fig. 7c. According to the forward scan response and since cathodic peaks were absent, the current recorded cannot be associated with any faradaic process related to CO$_2$ reduction reaction (CO$_2$RR). At −2 V (vs. SHE), the current density, J$_{(-2V)}$, was −6.271 mA cm^{-2}, the lowest under CO$_2$-saturated electrolyte for the isostructural MOFs studied. Indeed, no anodic peaks related to any faradaic process that could have occurred during the forward scan were observed in the reverse scan.

The cyclic voltammogram of the Mg/Zn-MOF-74 sample is shown in Fig. 7d. It is worth mentioning that, unlike the other three electrocatalysts, Mg/Zn-MOF-74 was the only one that showed a lower onset potential in a CO$_2$-saturated electrolyte (−1.219 V (vs. SHE)) than in a N$_2$-saturated electrolyte (−1.041 V (vs. SHE)), thus showing a higher current density in CO$_2$-saturated electrolyte. In the reverse scan, there are two anodic peaks at −0.645 V vs SHE and 0.668 V vs SHE, respectively, related to the oxidation of NO$_3^-$-derived species [33,34].

In summary, although the peaks evidenced the reduction of NO$_3^-$ ions, there were contributions from both the CO$_2$ reduction reaction (CO$_2$RR) and the hydrogen evolution reaction (HER). A summary of the current densities achieved at −2 V vs. SHE in N$_2$- and
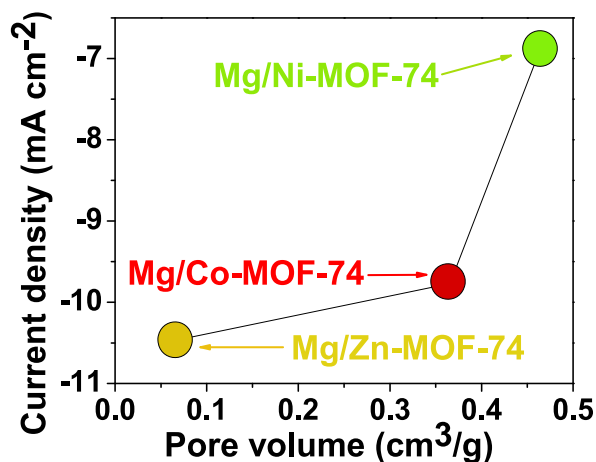
Fig. 9. Relationship between current density in CO_2-saturated electrolyte and pore volume of the bimetallic MOF-74 isostructural electrocatalysts.

CO_2-saturated electrolyte is presented in Table 3. Comparing the current densities among MOFs, the electrocatalyst Mg/Zn-MOF-74 showed the highest current density under CO_2-saturated electrolyte. As mentioned above, its onset potential under CO_2-saturated electrolyte was lower (-1.041 V vs. SHE) than its onset potential under N_2-saturated electrolyte (-1.219 V vs. SHE), as shown in Fig. 7, a fact that is favorable since the CO_2 reduction reaction itself consumes less energy. The results related to charge-transfer will be discussed in the following lines, evidencing the contribution of the CO_2 reduction reaction. According to the results of cyclic voltammetry in CO_2-saturated electrolyte, the bimetallic MOFs showed higher electrocatalytic activity for CO_2RR compared to the performance of monometallic Mg-MOF-74 performance, which demonstrated the lowest activity and Mg/Zn-MOF-74 particularly showed the best electrocatalytic activity in CO_2-saturated electrolyte.

3.7.2. Electrochemical impedance spectroscopy

Fig. 8a shows Nyquist plots obtained for the Mg/Co-MOF-74 sample in N_2-saturated and 0.1 M CO_2-saturated KNO_3 electrolyte, along with their respective fits attached for each of the equivalent circuits in Fig. 8b and c. Comparing the values extracted from the circuit elements, the values for the electrolyte resistance, R_Ω, and the charge transfer resistance, R_{CT}, increased slightly in the CO_2-saturated electrolyte. Therefore, there is a slight decrease in the admittance of the constant-phase element in the CO_2-saturated electrolyte. In addition, the increase in the double-layer capacitance can be attributed to a pH change from alkaline in the N_2-saturated electrolyte to acidic in the CO_2-saturated electrolyte. From the impedance plot shown in Fig. 8a, it is observed that the slope of the N_2-saturated electrolyte is steeper than the CO_2-saturated slope. This trend was also observed for the MOF samples Mg/Ni-MOF-74 and monometallic Mg-MOF-74 (see data shown in Figs. S6a–f of supporting information).

Fig. 8e and f shows equivalent circuits defined from impedance data fit for Mg/Zn-MOF-74. In contrast to the previous results for Mg/Co-MOF-74, Mg/Ni-MOF-74 and monometallic Mg-MOF-74, the electrolyte resistance, R_Ω, and the constant-phase element admittance, Y_0, decreased and increased in the CO_2-saturated electrolyte, respectively. Notably, the electrical double-layer capacitance, C_{DL}, decreased in the CO_2-saturated electrolyte.

Considering the results of textural properties, especially those of Mg/Zn-MOF-74, there must be a relationship between pore volume and a decrease in double-layer capacitance. According to the Mg content shown in Fig. 1b, d, f., the higher the Mg content on the bimetallic MOF-74, the lower the pore volume, as shown in Fig. 9. Due to the tunable pore size nature of the MOFs, these results suggest that Mg could be responsible for tuning the pore volume of the bimetallic MOF-74 electrocatalysts. As mentioned above, the Mg/Zn-MOF-74 has a large number of mesopores for a favorable mass transfer during the electrocatalytic process. Conversely, the BET surface area was not a critical parameter for the electrocatalytic activity in the reduction of CO2. The Mg/Zn-MOF-74 showed the lowest surface area, but the highest CO_2-derived electrocatalytic activity. This is due to the lower charge-transfer resistance observed in the Nyquist plot in the CO_2-saturared electrolyte, which was advantageous for higher electronic interaction during CO_2 electroreduction (Fig. 8d) [35]. From our samples, we found that Mg/Zn-MOF-74 had the smallest pore volume and a broader hysteresis loop, in contrast to the results of Mg/Co-MOF-74, Mg/Ni-MOF-74, and monometallic Mg-MOF-74, respectively. Notably, for the Nyquist plot of the Mg/Zn-MOF-74 electrocatalyst, it is observed that the slope of the CO_2-saturated electrolyte is now steeper than the slope of the N_2-saturated electrolyte (Fig. 8d), which may be related to less resistive behavior [36]. Accordingly, a narrower pore volume hinders the penetration of ions into the pores in a CO_2-saturated electrolyte, so the resulting ion layer at the electrode/electrolyte interface is less thick than in the N_2-saturated electrolyte, which in turn leads to a decrease in the capacitive current, which decreases the onset potential and allows a higher current density to be achieved in the CO_2-saturated electrolyte than that achieved in the N_2-saturated electrolyte, as reflected in Fig. 7 and its data summarized in Table 3. In fact, its pore network allowed CO_2 to diffuse more easily within the MOF than hydrogen produced from the concomitant reaction, thus decreasing the onset potential in the CO_2-saturated electrolyte. The highest CO_2-derived electrocatalytic activity corresponded to the Mg/Zn-MOF-74, which qualitatively had the highest Mg content in its lattice, tuning its pores and thus favoring the mass transfer of CO_2 molecules towards the MOF. We suggest that due to their
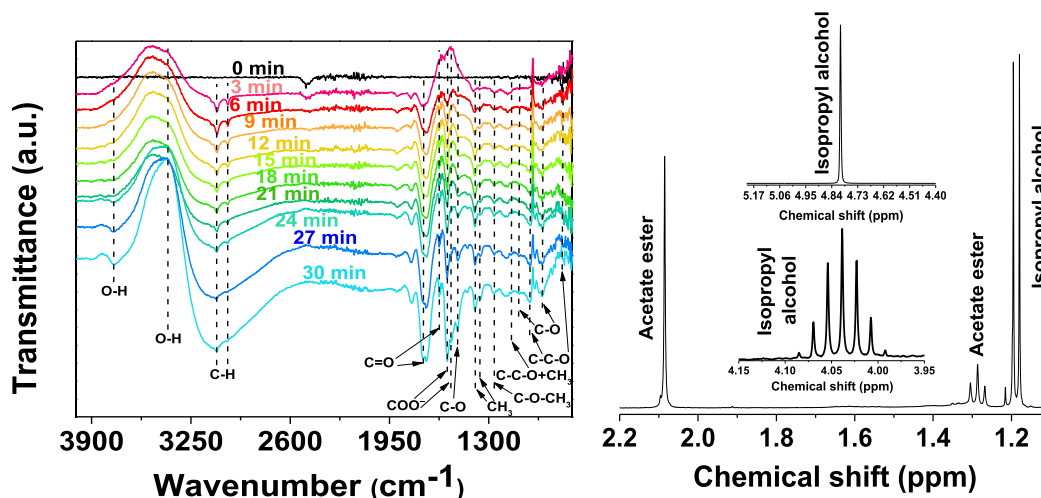
Fig. 10. Left: *In situ* FTIR spectrum of CO_2 reduction reaction on Mg/Ni-MOF-74 at −1.6 V vs. GE. Right: ^{1}H NMR spectra of the CO_2-saturated electrolyte taken after 1800 s (30 min) electrocatalysis over Mg/Ni-MOF-74 at −1.6 V vs. GE; The inset is the magnified part of the septet peak of isopropyl alcohol at δ4.04 ppm and the hydroxyl proton singlet at δ4.80 ppm.

coordination nature with the organic ligand during the synthesis process, Ni- and Co-derived bimetallic MOFs exhibited a limiting Mg loading during the synthesis process.

3.8. Spectroelectrochemical characterization of CO_2RR products

The stability of the MOFs was evaluated by chronoamperometry tests by recording the faradaic current generated at −1.6 V vs. SHE (Fig. S7 of supporting information). The following current density trend is verified: monometallic Mg < Mg/Ni < Mg/Co < Mg/Zn, previously attested in the CO_2-saturated cyclic voltammetry results. By checking these results, it is confirmed that there is a negligible faradaic current for monometallic Mg.

It is worth mentioning that when monometallic M-MOF-74 (M = Ni, Co and Zn) series were used as electrocatalysts under CO_2-saturated electrolyte, CO_2 was mainly reduced to CO (not shown here). These results are in agreement with those reported by Choi, I. et al. [15].

3.8.1. CO_2RR products obtained from Mg/Ni-MOF-74 electrocatalyst

The spectroelectrochemical results using Mg/Ni-MOF-74 electrocatalyst are shown in Fig. 10. The peak observed in the first scan at 2341 cm^{-1} corresponds to the asymmetrical stretching mode of CO_2 dissolved in the aqueous electrolyte, and its intensity decreased from the first scan, suggesting its consumption over time. The bands around 3755 cm^{-1} and 3400 cm^{-1} were associated with the O–H stretching of the alcohol [37], classified as a secondary alcohol due to the stretching vibration of the C–O single-bond appearing at 1100 cm^{-1} [38]. The bands appearing at 818 cm^{-1}, 953 cm^{-1} and 1153 cm^{-1} were attributed to the stretching of the C–C–O backbone, whose carbons correspond to methyl groups attached to the structure, which occurs prominently for isopropyl alcohol [38,39]. However, the most prominent and distinguishable peak confirming the presence of isopropyl alcohol in the liquid product is the one near 1380 cm^{-1}, split at 1391 cm^{-1} and 1356 cm^{-1}, attributed to an in-phase bending of the germinal dimethyl group [37,40]. To further confirm this statement, the ^{1}H NMR spectrum of this liquid product is shown in Fig. 10. The splitting patterns are a septet at δ4.04 ppm and a doublet at δ1.18 ppm, which is typical for an isopropyl group: the methyl protons give an upward doublet. In turn, the methine proton is split into a septet in the lower field by the six methyl protons. The hydroxyl proton signal appears as a singlet at δ4.7 ppm. Reciprocal coupling constants were carried on this splitting pattern, and it was found that both the doublet and the septet have a calculated coupling constant of 6.2 Hz, therefore, these multiplets are related to each other because they arise from reciprocal spin-spin couplings. This result confirms the presence of isopropyl alcohol in the liquid product.

In addition to isopropyl alcohol, there are other bands in the FTIR spectrum worth examining: there are stretching vibrations that suggest another liquid product having a carbonyl group. There is a sharp, medium-to-strong band appearing at 1730 cm^{-1}, a stretching vibration frequency commonly noted for aliphatic esters [37]. To elucidate the carbonyl-containing product, the ^{1}H NMR spectrum confirms that ester acetate is the carbonyl-containing CO_2-derived by-product. The ester acetate has a methyl singlet at δ2.08 ppm as a methyl group appears ca. δ2.0 ppm when attached to the carbonyl group and a terminal methyl group cleaved by a neighboring methyl group into a triplet centered at δ1.28 ppm. In addition to ester acetate and isopropyl alcohol, formic acid was another carbonyl-containing product that appeared in the ^{1}H NMR spectra as a singlet centered at δ8.37 ppm, as shown in Fig. S8 (supporting information). Its presence is confirmed by infrared absorption at 1571 cm^{-1} and 1547 cm^{-1} attributed to COO$^-$ ions [41]. This is in good agreement with Shao-Hong et al. CO_2-derived product (formate) using MgNi-MOF-74 as the photocatalyst [9].
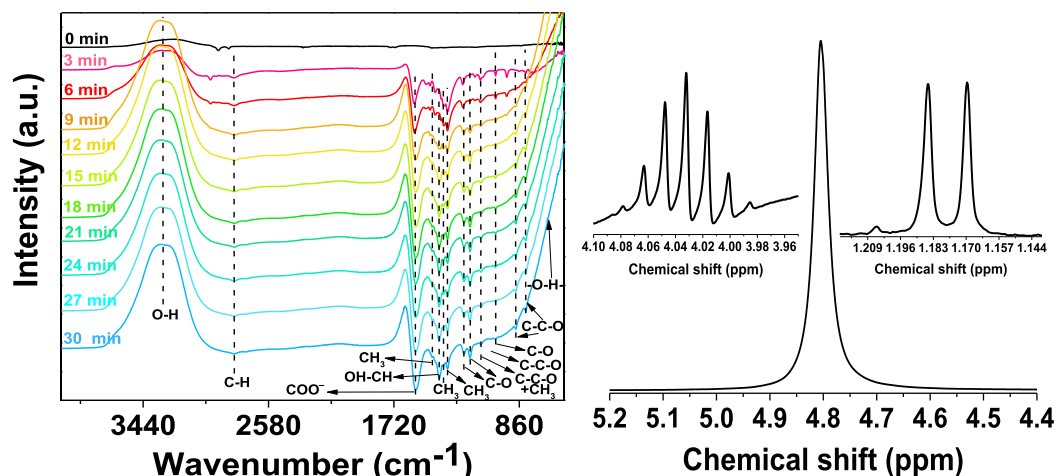
Fig. 11. Left: *In situ* FTIR spectra of CO_2 reduction reaction on Mg/Co-MOF-74 at −1.6 V vs. GE. Right: ^1H NMR spectra of the CO_2-saturated electrolyte taken after 1800 s (30 min) electrocatalysis over Mg/Co-MOF-74 at −1.6 V vs. GE; The inset is the magnified part of the septet peak of isopropyl alcohol at 4.04 ppm and the hydroxyl proton singlet at δ4.80 ppm.

Fig. 12. Left: *In situ* FTIR spectra of CO_2 reduction reaction on Mg/Zn-MOF-74 at −1.6 V vs. GE. Right: ^1H NMR spectra of the CO_2-saturated electrolyte taken after 1800 s (30 min) electrocatalysis over Mg/Zn-MOF-74 at −1.6 V vs. GE; The inset is the magnified part of the septet peak of isopropyl alcohol at 4.04 ppm and the hydroxyl proton singlet at δ4.80 ppm.
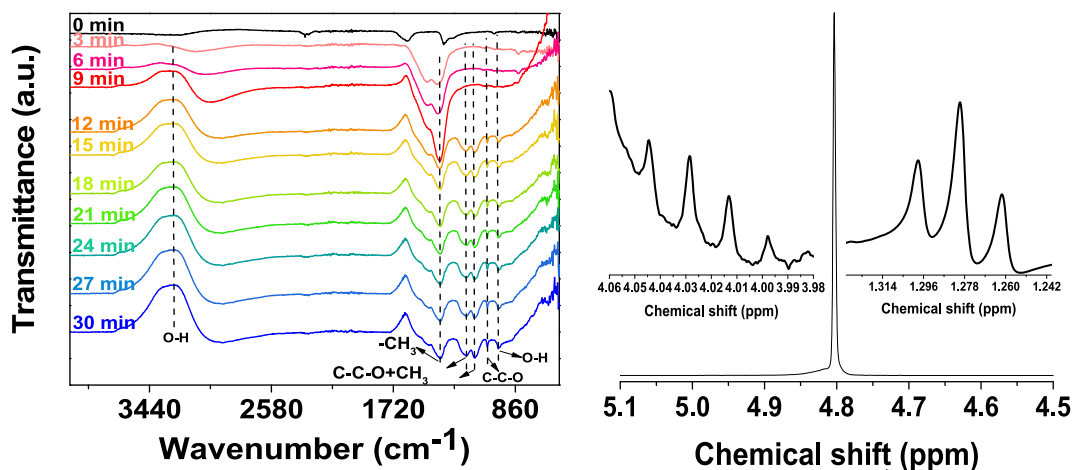
3.8.2. CO2RR products obtained from Mg/Co-MOF-74 electrocatalyst

The Fig. 11 presents the *in situ* FTIR spectra of collected Mg/Co-MOF-74 under CO_2-saturated KOH 0.1 M electrolyte at −1.6 V vs. GE. The band around 3318 cm^{-1} was associated with the O–H stretching of alcohol [37]. The peaks at 1242 cm^{-1}, 1196 cm^{-1}, 1023 cm^{-1}, 885 cm^{-1} and 816 cm^{-1} are ascribed to C–O stretching vibrations [38,39]. Furthermore, the C–O–C stretching vibration at 1125 cm^{-1} is linked to a CH_3 rocking motion [38]. There is a C–O–C stretch at 1058 cm^{-1} typically ascribed for a primary alcohol, yet at the last scan it is significantly weak, suggesting that a primary alcohol is not expected to be the main liquid product. However, there is a pattern of doublets assigned to in-phase CH_3 bending motions observed in compounds with isopropyl groups at 1380 cm^{-1} and 1352 cm^{-1} [37,38,40], suggesting that isopropyl alcohol is the main CO_2-derived liquid product. Indeed, the infrared absorption peaks at 1463 cm^{-1}, 1415 cm^{-1} and 663 cm^{-1} are observed for isopropyl alcohol, as 1415 cm^{-1} is ascribed to OH–CH bending, 1463 cm^{-1} is attributed to –CH_3 out-of-phase bending and 663 cm^{-1} is attached to O–H wagging motion, respectively [38]. ^1H Nuclear magnetic resonance spectroscopy (^1H NMR) confirmed the presence of the characteristic isopropyl group. The ^1H NMR spectrum acquired in the electrolyte reveals a typical doublet-septet pattern of an isopropyl group, as discussed above. These results indicated that isopropyl alcohol is the secondary alcohol observed in the FTIR spectra and could be the main liquid CO_2-derived product for Mg/Co-MOF-74.

3.8.3. CO2RR products obtained using Mg/Zn-MOF-74 electrocatalyst

Fig. 12 presents the *in situ* FTIR spectra of Mg/Zn-MOF-74 collected under CO_2-saturated KOH 0.1 M electrolyte at −1.6 V vs. GE. The most conspicuous feature is a broad band around 3272 cm^{-1} due to the O–H stretching of hydrogen-bonded alcohol groups [38].
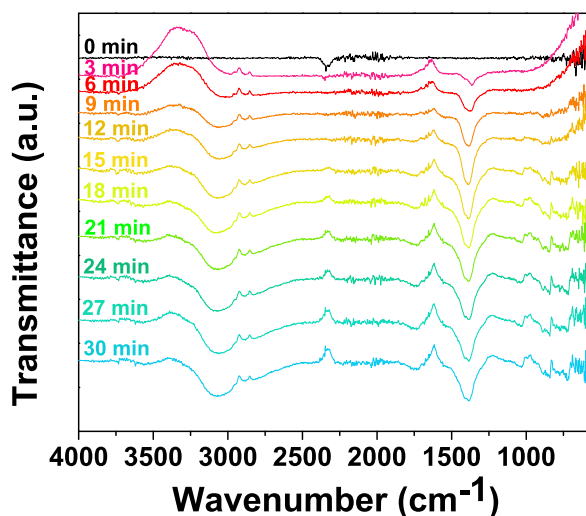
Fig. 13. Left: *In situ* FTIR spectra of CO_2 reduction reaction on Mg-MOF-74 at −1.6 V vs. GE. Right: NMR spectra of the CO_2-saturated electrolyte taken after 1800 s (30 min) electrocatalysis over Mg-MOF-74 at −1.6 V vs. GE.

The O–H deformation features a sharp peak at 981 cm^{-1} [37]. There is evidence for C–C–O skeletal vibration at 1206 cm^{-1}, 1148 cm^{-1} and 1056 cm^{-1} [37,38]. The latter reveals the nature of alcohol as a primary alcohol. Carbon-hydrogen stretching vibrations appear at 2924 cm^{-1}, whereas peaks at 1467 cm^{-1} and 1390 cm^{-1} were ascribable to –CH_3 out-of-phase and in-phase stretching vibrations, respectively [38]. ^{1}H NMR spectrum acquired on the electrolyte reveals a triplet-quartet splitting pattern at δ1.28 ppm and δ4.03 ppm, respectively. This splitting pattern is typical for an ethyl group, as the higher-field triplet arises from the methyl group and the quartet at lower field arises from O–CH_2, as oxygen atoms are σ-withdrawers of electron density, deshielding protons on the adjacent carbon atom. There is also a singlet featuring at δ4.8 ppm due to the hydroxyl proton. Considering this information, it can be therefore concluded that the primary alcohol observed is ethanol.

3.8.4. CO₂RR analysis using monometallic Mg-MOF-74 compound

Fig. 13 presents the *in situ* FTIR spectra of Mg-MOF-74 collected under CO_2-saturated KOH 0.1 M electrolyte at −1.6 V vs. GE. The spectral feature at 1380 cm^{-1} appears to arise from surface carbonate species, specifically to the carbonate ion due to the antisymmetric C–O stretch [41,42]. It is notorious that there are no peaks suggesting the presence of carbonyl-containing groups or hydrogen-bonded alcohol groups in the liquid product. Moreover, the asymmetrical stretching mode of dissolved CO_2 in the aqueous electrolyte has positive-going orientation as the scans span. Compared to the transition-metal-containing MOF spectra, Mg-MOF-74 spectrum (Fig. 13) clearly evidenced it was unable to reduce CO_2 to an organic-derived product, yet it only undergoes carbon mineralization [43,44].

4. Conclusions

Four types of isostructural MOF-74 electrocatalysts were successfully synthesized under solvothermal conditions. The contrasting Mg content on each of the bimetallic MOFs revealed the preferential coordination of Ni^{2+} and Co^{2+} ions with the H_4DOBDC ligand over Mg^{2+} ions, resulting in a limited Mg content loaded on Mg/Ni- and Mg/Co-MOF-74 samples. On the other hand, the coordination of Zn^{2+} ions with the H_4DOBDC ligand did not limit Mg^{2+} ions, resulting in a higher Mg content in Mg/Zn-MOF-74 responsible for tuning the pore network of the sample. This results in the appearance of mesopores, which are advantageous for the mass transfer during the CO_2 electroreduction process. This statement was further supported by the less resistive behavior of its Nyquist plot in CO_2-saturated electrolyte, as well as by its double-layer capacitance value. According to cyclic voltammetry and chronoamperometric tests, the bimetallic MOF-74 electrocatalysts exhibited higher electrocatalytic activity for CO_2 than the monometallic Mg-MOF-74 electrocatalysts, which did not show any C_2-deep reduction CO_2 derived product. In fact, Mg/Zn-MOF-74 had the highest CO_2-derived electrocatalytic activity. In situ ATR-FTIR measurements and structure elucidation by ^{1}H NMR have shown that all of the bimetallic electrocatalysts reduce CO_2 to C_2 deep-reduction products. Mg/Ni-MOF-74 produced formic acid, isopropyl alcohol, and an ester acetate, which is very rare to obtain from CO_2, whereas Mg/Co-MOF-74 and Mg/Zn-MOF-74 produced isopropyl alcohol and ethanol, respectively.

Author contribution statement

Rodrigo Andrés Espinosa-Flores: Performed the experiments; Analyzed and interpreted the data; Wrote the paper. Martin Daniel Trejo Valdez: Conceived and designed the experiments. María Elena Manríquez Ramírez: Analyzed and interpreted the data. Francisco

Javier Tzompantzi Morales: Contributed reagents, materials, analysis tools or data.

Data availability statement

Data included in article/supp. Material/referenced in article.

Declaration of competing interest

The authors declare that they have no known competing financial interests or personal relationships that could have appeared to influence the work reported in this paper.

Acknowledgements

Appendix A. Supplementary data

Supplementary data related to this article can be found at https://doi.org/10.1016/j.heliyon.2023.e17138.

References

[1] M. Asgari, W. Queen, Carbon capture in metal-organic frameworks, in: L. Li, W. Wong-Ng, K. Huang, L.P. Cook (Eds.), Materials and Processes for CO_2 Capture, Conversion, and Sequestration, Wiley, Switzerland, 2018, pp. 1–63.

[2] M. Aulice Scibioh, B. Viswanathan, Electrochemical reduction of carbon dioxide: a status report, Proc. Indian Natl. Sci. Acad. 70 (3) (2004) 407–462.

[3] K. Lai, S. Ci, Z. Wen, Nanoelectrocatalysts for carbon dioxide reduction reduction, in: X. Luo, F. Deng (Eds.), Nanomaterials for the Removal of Pollutants and Resource Reutilization, Elsevier Inc, 2019, pp. 243–268.

[4] G. Keerthiga, P. Karthik, B. Neppolian, Application of metal-organic framework and their derived materials, in: Inamuddin En, R. Boddula, M.I. Ahamed, A. M. Asiri (Eds.), Applications of Metal-Organic Frameworks and Their Derived Materials, Scrivener Publishing, Wiley, Hoboken, Nueva Jersey, 2020, pp. 357–376.

[5] K. Gopalram, K. Peramaiah, N. Bernaurdshaw, Application of metal-organic framework and their derived materials in electrocatalysis, in: Inamuddin, R. Boddula, M.I. Ahamed, A.M. Asiri (Eds.), Application of Metal-Organic Framework and Their Derived Materials in Electrocatalysis, Scrivener Publishing LLC, Beverly, Massachusetts, 2020, pp. 357–376.

[6] P. Cai, W. Chen, G.S. Day, H.F. Drake, E.A. Joseph, Z.T. Perry, Z. Xiao, H. Zhou, Metal-organic frameworks: new functional materials and applications, in: D. L. Andrews, R.H. Lipson, T. Nann (Eds.), Comprehensive Nanoscience and Technology, ElSevier B. V., 2019, pp. 35–54.

[7] Y. Zhao, et al., Nanoengineering metal-organic framework-based materials for use in electrochemical CO_2 reduction reactions, Small 17 (16) (2021), 2006590.

[8] J. Ling, et al., One-pot method synthesis of bimetallic MgCu-MOF-74 and its CO_2 adsorption under visible light, ACS Omega 2022 (7) (2022) 19920–19929.

[9] G. Shao-Hong, et al., A bimetallic-MOF catalyst for efficient CO_2 photoreduction from simulated flue gas to value-added formate, J. Mater. Chem. 2020 (8) (2020), 11712.

[10] D. Narvaez-Celada, A.S. Varela, CO_2 electrochemical reduction on metal-organic framework catalysts: current status and future directions, J. Mater. Chem. 2022 (10) (2022) 5899–5917.

[11] S.S.A. Shah, T. Najam, M. Wen, S.-Q. Zang, A. Waseem, H.-L. Jiang, Metal-organic framework-based electrocatalysts for CO_2 reduction, Small Struct. 2022 (3) (2022), 2100090.

[12] K. Sumida, et al., Carbon dioxide capture in metal-organic frameworks, Chem. Rev. 2012 (112) (2012) 724–781.

[13] Z. Gao, et al., Facile one-pot synthesis of Zn/Mg-MOF-74 with unsaturated coordination metal centers for efficient CO_2 adsorption and conversion to cyclic carbonates, ACS Appl. Mater. Interfaces 13 (51) (2021) 61334–61345.

[14] P. Shao, L. Yi, S. Chen, T. Zhou, J. Zhang, Metal-organic frameworks for electrochemical reduction of carbon dioxide: the role of metal centers, J. Energy Chem. 40 (2020) (2019) 156–170.

[15] I. Choi, et al., Facile synthesis of M-MOF-74 (M = Co, Ni, Zn) and its application as an ElectroCatalyst for electrochemical CO_2 conversion and H_2 production, J. Electrochem. Sci. Technol. 8 (1) (2017) 61–68.

[16] S.R. Caskey, et al., Dramatic tuning of carbon dioxide uptake via metal substitution in a coordination polymer with cylindrical pores, J. Am. Chem. Soc. 2008 (130) (2008) 10870–10871.

[17] Z. Lv, et al., Enhanced removal of uranium (VI) from aqueous electrolyte by a novel Mg-MOF-74-derived porous MgO/carbon adsorbent, J. Colloid Interface Sci. 537 (2019) A1–A10.

[18] M.F. Sanad, et al., Co-Cu bimetallic metal organic framework catalyst outperforms the Pt/C benchmark for oxygen reduction, J. Am. Chem. Soc. 143 (10) (2021) 4064–4073.

[19] M. Zhang, et al., Preparation of NiCo-MOF-74 and its electrocatalytic oxygen precipitation performance, J. Beijing Univ. Chem. Technol. 46 (4) (2019) 38–45.

[20] T. Yang, et al., Preparation of M-MOF-74 (M = Ni, Co, Zn) and its performance in electrocatalytic synthesis of ammonia, CIESC J. 71 (6) (2020) 2857–2870.

[21] Y. Wang, S. Nie, Y. Liu, W. Yan, S. Lin, G. Cheng, H. Yang, J. Luo, Room-temperature fabrication of a nickel-functionalized copper metal-organic framework (Ni@Cu-MOF) as a new pseudocapacitive material for asymmetric supercapacitors, Polymers 11 (5) (2019) 821.

[22] Y. Gong, L. Jiao, Y. Qian, C. Pan, L. Zheng, X. Cai, B. Liu, S. Yu, H. Jiang, Regulating the coordination environment of MOF-templated single-atom nickel electrocatalysts for boosting CO_2 reduction, Angew. Chem. Int. Ed. 59 (2020) 2705–2709.

[23] H. Furukawa, Synthesis and characterization of metal-organic frameworks, in: T.G. Glover, B. Mu (Eds.), Gas Adsorption in Metal-Organic Frameworks, CRC Press/Taylor & Francis Group, Boca Raton, Florida, 2019, pp. 17–81.

[24] P. Yurkanis, Química Orgánica, fifth ed., Pearson Educación, 2008.

[25] N. Iswarya, et al., Synthesis, characterization and adsorption capability of MOF-5, Asian J. Sci. Res. 5 (4) (2012) 247–254.

[26] D.T.C. Nguyen, et al., Metal-organic framework MIL-53 (Fe) as an adsorbent for ibuprofen drug removal from aqueous electrolytes: response surface modeling and optimization, Hindawi J. Chem. 2019 (2019) 1–11.

[27] K.H. Tan, Humic Matter in Soil and the Environment. Principles and Controversies, Marcel Dekker, Inc., 2003.

[28] M.B. Smith, Organic Chemistry: an Acid—Base Approach, CRC Press. Taylor & Francis Group, 2011.

[29] L. Wade, Organic Chemistry seventh ed., Vol. 1, Pearson Educación, 2011.

[30] E.F. Sousa-Aguiar, P.A. Arroyo, M.A. Simões Dornellas de Barros, J. Lopes de Miranda, The future of zeolite and MOF materials, in: V. Blay, L.F. Bobadilla, A. Cabrera Garcia (Eds.), Zeolites and Metal-Organic Frameworks, Amsterdam University Press, 2018, p. 330.

[31] S. Xie, Q. Qin, H. Liu, L. Jin, X. Wei, J. Liu, X. Liu, Y. Yao, L. Dong, B. Li, MOF-74-M (M = Mn, Co, Ni, Zn, MnCo, MnNi, and MnZn) for low-temperature NH_3-SCR and in situ DRIFTS study reaction mechanism, ACS Appl. Mater. Interfaces 12 (43) (2020) 48476–48485.

[32] R. Senthil Kumar, et al., Highly selective electrochemical reduction of carbon dioxide using Cu based metal organic framework as an electrocatalyst, Electrochem. Commun. 25 (2012) 70–73.

[33] S. Amertharaj, et al., Electroreduction of nitrate ions at a platinum-copper electrode in an alkaline medium: influence of sodium inositol phytate, Electrochim. Acta 136 (2014) 557–564.

[34] M.A. Hasnat, et al., Copper-immobilized platinum electrocatalyst for the effective reduction of nitrate in a low conductive medium: mechanism, adsorption thermodynamics and stability, Appl. Catal. Gen. 478 (2014) 259–266.

[35] K. Zhao, et al., CO_2 electroreduction at low overpotential on oxide-derived Cu/carbons fabricated from metal organic framework, ACS Appl. Mater. Interfaces 9 (6) (2017) 5302–5311.

[36] V.F. Lvovich, Equivalent circuits modeling of the impedance phenomenon, in: V.F. Lvovich (Ed.), Impedance Spectroscopy: Applications to Electrochemical and Dielectric Phenomena, John Wiley & Sons, Inc., 2019, pp. 37–48.

[37] G. Socrates, Infrared and Raman Characteristic Group Frequencies: Tables and Charts, third ed., Wiley, 2004.

[38] P.J. Larkin, Infrared and Raman spectroscopy, in: Principles and Spectral Interpretation, Elsevier, 2011.

[39] B.C. Smith, Infrared Spectral Interpretation. A Systematic Approach, CRC Press, 1999.

[40] D.L. Pavia, G.M. Lampman, G.S. Kriz, J.R. Vyvyan, Introduction to Spectroscopy, fifth ed., Cengage Learning, 2015.

[41] K.D. Dobson, A.J. McQuillan, An infrared spectroscopic study of carbonate adsorption to zirconium dioxide sol-gel films from aqueous solutions, Langmuir 1997 (13) (1997) 3392–3396.

[42] Y. Kohno, et al., Photoreduction of carbon dioxide by hydrogen over magnesium oxide, Phys. Chem. Chem. Phys. 2001 (3) (2001) 1108–1113.

[43] G. Gadikota, Carbon mineralization pathways for carbon capture, storage and utilization, Commun. Chem. 4 (23) (2021).

[44] A. Alturki, The global carbon footprint and how new carbon mineralization technologies can Be used to reduce CO_2 emissions, ChemEngineering 6 (44) (2022).